

We are IntechOpen, the world's leading publisher of Open Access books Built by scientists, for scientists

6,900

Open access books available

186,000

International authors and editors

200M

Downloads

Our authors are among the

154

Countries delivered to

TOP 1%

most cited scientists

12.2%

Contributors from top 500 universities



WEB OF SCIENCE™

Selection of our books indexed in the Book Citation Index
in Web of Science™ Core Collection (BKCI)

Interested in publishing with us?
Contact book.department@intechopen.com

Numbers displayed above are based on latest data collected.
For more information visit www.intechopen.com



Structural, Morphological, Magneto-Transport and Thermal Properties of Antimony Substituted $(\text{La,Pr})_{2/3}\text{Ba}_{1/3}\text{Mn}_{1-x}\text{Sb}_x\text{O}_3$ Perovskite Manganites

Neeraj Panwar¹, Indrani Coondoo¹, Vikram Sen^{2,3} and S. K. Agarwal²

¹*Departamento de Ceramica e Engenharia do Vidro & CICECO, Universidade de Aveiro*

²*National Physical Laboratory, (CSIR), Dr. K. S. Krishnan Marg, New Delhi*

³*Bhagwati Institute of Technology & Science, Masuri - Ghaziabad, UP*

¹*Portugal*

^{2,3}*India*

1. Introduction

Magneto-resistance (MR) is generally defined as the relative change in the electrical resistivity of a material upon the application of magnetic field. Mathematically, MR can be defined by the following equation,

$$MR(\%) = \left[\frac{\rho_0 - \rho_H}{\rho_H} \right] \times 100 \quad (1)$$

where ρ_H and ρ_0 are the electrical resistivities with and without magnetic field respectively. Electrical resistivity can increase or decrease upon the application of magnetic field and accordingly MR is defined as positive or negative respectively. By using the above definition observed MR could be $\sim 10^6\%$ or even higher, but if we define MR by the following relation,

$$MR(\%) = \left[\frac{\rho_0 - \rho_H}{\rho_0} \right] \times 100 \quad (2)$$

then maximum MR will be $\sim 100\%$.

W. Thomson (Lord Kelvin) in 1857, for the first time, discovered magneto-resistance¹. All metals exhibit MR due to Lorentz force but the value of MR is only few percent even after the application of higher magnetic field. For example, Cu metal exhibits 1% MR at room temperature under 7 Tesla applied magnetic field. In the case of ferromagnetic metals like Fe and Co, MR is more ($\sim 15\%$) as compared to that of nonmagnetic metals such as gold (Au). Semimetal bismuth (Bi) shows about 18% MR in a transverse magnetic field of 0.6T and 250% MR at room temperature under the application of 5 Tesla magnetic field².

In search of higher MR values near room temperatures, the last two decades have witnessed the discovery of an enormous suppression in electrical resistivity upon the application of

magnetic field in certain class of materials called manganites. The observed change was so large that a special name “colossal magneto-resistance (CMR)” had to be coined for this phenomenon to distinguish it from the already existing giant magneto-resistance (GMR) in the magnetic multilayers. For example, Chahara et al.³, R. von Helmolt et al.⁴, Jin et al.⁵, Xiong et al.⁶ have reported $\sim 10^6$ % MR under the application of 6T magnetic field. Searle and Wang et al.^{7, 8} were the first to report MR studies in $\text{La}_{1-x}\text{Pb}_x\text{MnO}_3$ single crystal manganites. The renewed surge of interest in manganites in the 1990s started with the experimental observation of large magneto-resistance (MR) studies in $\text{Nd}_{0.5}\text{Pb}_{0.5}\text{MnO}_3$ by Kusters et al.⁹ and in $\text{La}_{2/3}\text{Ba}_{1/3}\text{MnO}_3$ by R. von Helmolt et al.⁴. MR effect was found to be as high as 60% (using eq. 2) in thin films at room temperature, and it was exciting to observe that this value was higher than found in artificial magnetic/nonmagnetic multilayers i.e. Giant magneto-resistive materials (GMR)¹⁰, allowing for potential applications in magnetic recording. Thereafter Chahara et al.³ on $\text{La}_{3/4}\text{Ca}_{1/4}\text{MnO}_3$ and Ju et al.¹¹ on $\text{La}_{1-x}\text{Sr}_x\text{MnO}_3$ films produced similar results. Jin et al.⁵ observed 127,000% around 77K using Eq. (1) for defining MR in thin films of $\text{La}_{0.67}\text{Ca}_{0.33}\text{MnO}_3$ and Xiong et al.⁶ 100,000% in $\text{Nd}_{0.7}\text{Sr}_{0.3}\text{MnO}_3$ film at 60K.

1.1 Crystal structure

Rare-earth manganites possess a perovskite crystal structure (Fig. 1a) with the general formula $\text{R}_{1-x}\text{A}_x\text{MnO}_3$, where R is any trivalent rare-earth ion like La^{+3} , Pr^{+3} , Nd^{+3} , Eu^{+3} etc. and A is divalent alkaline-earth ion (Ca^{+2} , Sr^{+2} , Ba^{+2} etc.) whereas x represents the amount of doping of such divalent ions at the rare-earth site and equal number of Mn^{+3} -ions are converted into Mn^{+4} - ions. The mixed valency of manganese ions can also be controlled by varying the oxygen content^{12,13}. In the perovskite structure each manganese (Mn) ion is surrounded by six oxygen ions forming an octahedron (Fig. 1a).

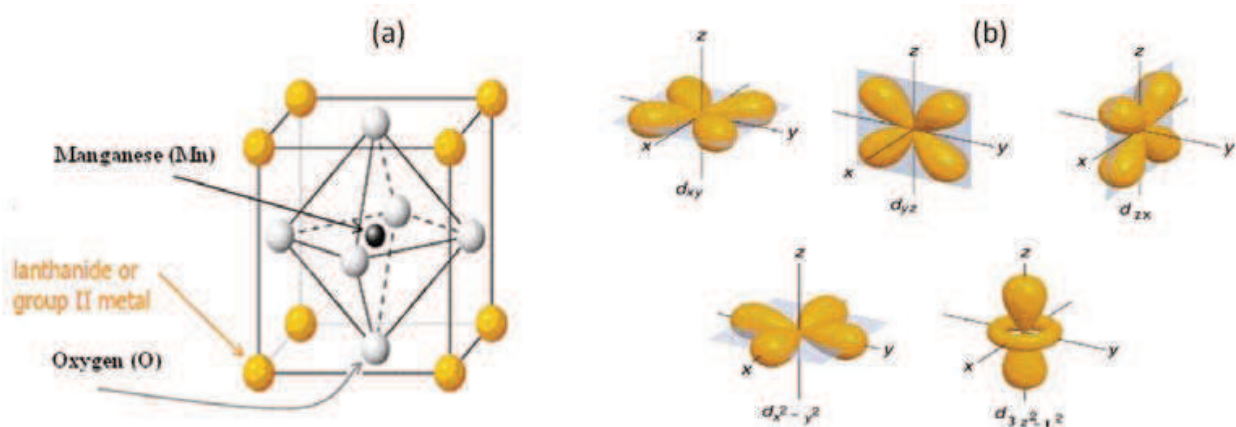


Fig. 1. (a) arrangements of ions in the perovskite structure of manganites. (b) shape of different d-orbitals.

In MnO_6 octahedron overlapping of manganese 3d orbitals with the 2p orbital of oxygen splits the five-fold degeneracy of the manganese 3d orbitals due to their different shapes (Fig. 1b). This is called crystal field splitting (CFS). Thus in an MnO_6 octahedron three degenerate orbitals (d_{xy} , d_{yz} , d_{zx}) with lower energy (because their lobes are oriented between the O^{2-} ions) are called t_{2g} levels and two degenerate orbitals ($d_{x^2-y^2}$, $d_{3z^2-r^2}$) with higher energy (their lobes are towards O^{2-} ions and hence large Coulomb repulsion) called e_g

levels¹⁴. Due to crystal field splitting the energy difference between t_{2g} and e_g levels is ~ 1.5 eV¹⁵. All electrons in these energy levels get aligned parallel to each other due to strong on-site Hund's coupling, leading to a total spin (S) of 2 for Mn^{+3} and $S = 3/2$ for Mn^{+4} ions respectively. The three electrons of Mn^{+4} - ion occupy t_{2g} states whereas fourth electron of Mn^{+3} goes to the e_g state. The e_g electrons are more itinerant than the t_{2g} electrons and can hop from one Mn-site to the other. However, according to Jahn-Teller (JT) theorem this configuration is not stable and the degeneracy of the e_g levels are further removed¹⁶. The oxygen ions surrounding the Mn^{+3} -ion slightly readjust their positions, creating an asymmetry in different directions which ultimately breaks the degeneracy. The breaking of degeneracy due to orbital-lattice interaction is called Jahn-Teller splitting (Fig. 2). Only those ions like Mn^{+3} which have odd number of electrons in the e_g levels can undergo Jahn-Teller distortion. Therefore Mn^{+3} is a Jahn-Teller ion whereas Mn^{+4} is not. In the case of manganites there are 21 degrees of freedom (modes of vibration) for the movement of oxygen and Mn ion¹⁷. Out of these only two types of distortion are relevant for the splitting of e_g levels i.e. Q_2 and Q_3 (Fig. 3)¹⁸. Q_2 is a basal plane distortion (defined as Q_2 mode) in which one diagonally O pair is displaced inwards whereas the other pair is displaced outwards. On the other hand, Q_3 is a tetragonal distortion which results in elongation or distortion of MnO_6 octahedron. JT distortion can be static or dynamic.

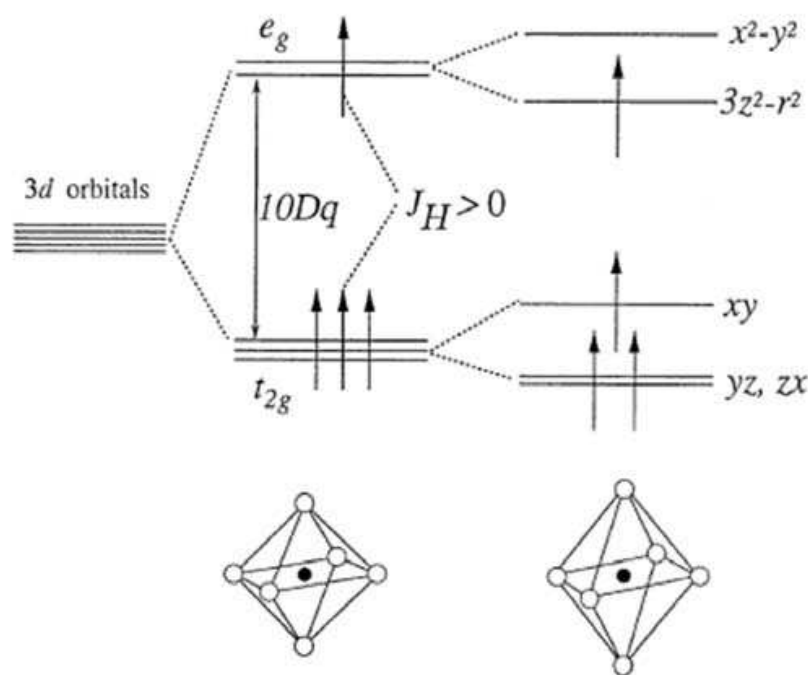


Fig. 2. Crystal field splitting of the five-fold degenerate atomic 3d levels into lower t_{2g} and higher e_g levels. Jahn-Teller distortion further lifts the degeneracy (from Tokura, 2000 [19]).

Perovskite manganites not only exhibit the colossal magnetoresistance (CMR) effect but also other important phenomena like charge ordering, phase separation at nanoscale owing to the subtle balance between charge, spin, lattice and orbital degrees of freedom¹⁹. As mentioned earlier, electrical resistivity of these manganites can change dramatically in response to an applied magnetic field. The occurrence of magneto-resistance can be explained by Zener's theory of double exchange along-with the formation of Jahn-Teller polarons²⁰. In order to understand magnetoresistance behavior and other peculiar properties

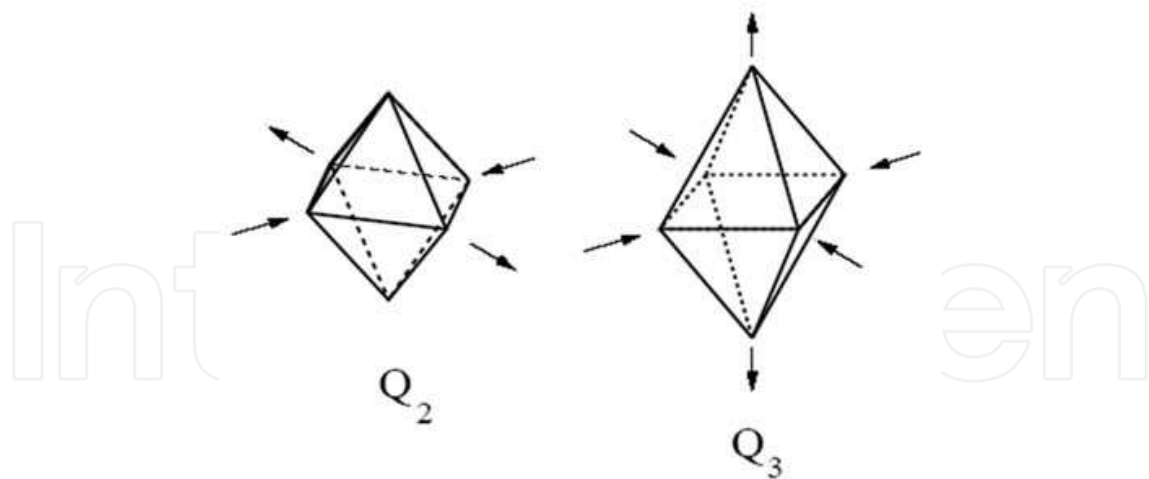


Fig. 3. Mode of vibrations Q_2 and Q_3 for the splitting of e_g doublet.

exhibited by these materials, substitution engineering is carried out either at the rare-earth site or at the manganese site. However, out of the two, the last is more appropriate as it directly affects the mechanism happening among different MnO_6 octahedra. In this regard, several authors have substituted different transition metal ions like Fe^{+3} , Al^{+3} , Ga^{+3} , Zn^{+2} , Cu^{+3} , Ni^{+2} at the Mn-site and have shown that Mn-site substitution severely affects the conduction mechanism as well as the magnetic properties²¹⁻²⁸. However, fewer results exist for higher valent ion substitution at Mn-site to see its effect on the transport properties²⁹⁻³³. Substitutions at Mn-sites in manganites, irrespective of their electronic and magnetic nature, lower the ferromagnetic transition temperature but to different extents except in the case of Ru-doped $Pr_{0.5}Sr_{0.5}MnO_3$ where it is found to increase with Ru³². In this work, we have attempted to substitute Sb^{+5} ion on the Mn-site in two different manganite materials *viz.* $La_{2/3}Ba_{1/3}MnO_3$ (LBMO) and $Pr_{2/3}Ba_{1/3}MnO_3$ (PBMO)³⁴⁻³⁸. Sb^{+5} ion has been chosen because its ionic size is also comparable to that of manganese ion in the six-fold co-ordination. Besides, by virtue of its closed shell configuration, Sb^{+5} ion is not expected to introduce any additional magnetic coupling. It is also not expected to participate explicitly in the mechanism between Mn^{+3}/Mn^{+4} ions, however, due to its filled shell structure it can hinder the electron transfer. We have carried out structural, morphological, electrical, magnetoresistive and thermal measurements on the aforementioned compositions and the results will be discussed here.

2. Experimental procedure

Bulk polycrystalline manganite samples of $La_{2/3}Ba_{1/3}(Mn_{1-x}Sb_x)O_3$ and $Pr_{2/3}Ba_{1/3}(Mn_{1-x}Sb_x)O_3$ ($0 \leq x \leq 0.03$) [referred hereafter as $(La, Pr)_{2/3}Ba_{1/3}(Mn_{1-x}Sb_x)O_3$] were synthesized following the conventional solid-state reaction method. Powders of La_2O_3 , Pr_6O_{11} , $BaCO_3$, Sb_2O_5 and MnO_2 were mixed in nominal stoichiometric ratios, grounded properly and calcined several times between 900-1100 °C for 15 h with intermediate grindings. Finally, the pellets were made from the calcined powders and sintered at 1260 °C for 20 h. X-ray diffraction (XRD) was carried out with $Cu K_\alpha$ radiation ($\lambda = 1.54 \text{ \AA}$) between 20° and 80° with a step size of 0.05° in 2θ mode to ascertain the phase purity of the synthesized materials. Electrical resistivity measurement in the absence and presence of a magnetic field was carried out using a four-probe technique with the field (0.6 T) applied

parallel to the direction of the current flow. Thermoelectric power $S(T)$ and thermal conductivity $\kappa(T)$ measurements were carried out simultaneously from 350 to 10K in a closed cycle refrigerator by using a direct-heat pulse technique. Specific heat $C_P(T)$ was measured from 350 to 77K with a high resolution ac calorimeter, using chopped light as heat source. Further details of the thermal measurements techniques can be found in ref.³⁹.

3. Results and discussion

3.1 Structural studies

Fig. 4 shows the x-ray diffractograms of $\text{La}_{2/3}\text{Ba}_{1/3}(\text{Mn}_{1-x}\text{Sb}_x)\text{O}_3$ and $\text{Pr}_{2/3}\text{Ba}_{1/3}(\text{Mn}_{1-x}\text{Sb}_x)\text{O}_3$ ($0 \leq x \leq 0.03$) series. All samples are single phase in nature. It is also clear that Sb^{5+} ion occupies the Mn-site in LBMO and PBMO. Substitutional criteria of valence, ionic size and the coordination assured the preferential occupation of Mn^{4+} ion site by Sb^{5+} ion. The parent compound LBMO possesses the cubic structure [lattice parameter = $3.9094(\pm 0.09\%) \text{ \AA}$] at room temperature. In refs.⁴⁰⁻⁴² the structure of LBMO has been reported cubic. In some reports neutron diffraction study has been carried out as a function of temperature on LBMO perovskite manganite and it has been deduced that it crystallizes in the rhombohedral structure (closer to cubic, space group R3c) at room temperature^{43,44}. However, the final sintering temperature in our case is $1260 \text{ }^\circ\text{C}$ while it is much higher as reported in ref. ⁴⁵(e.g. $1470 \text{ }^\circ\text{C}$ used by Beznosov et al. and $1400 \text{ }^\circ\text{C}$ by Moutis et al.) and such a high temperature can change the lattice structure from cubic to rhombohedral. With the subsequent doping of Sb^{5+} ion the lattice parameters increase successively [e.g. $3.9180 (\pm 0.011\%) \text{ \AA}$ for 3% Sb-doped sample] which indicates the occupation of Mn^{4+} ion by Sb^{5+} in LBMO. The increase in the lattice parameter is also evident as the main peak shifts towards lower 2θ values with increasing Sb-content. The lower value of 2θ implies higher d values and consequently higher lattice parameter. The increase in the lattice parameters can also be understood in terms of the increase of the mean ionic radius at Mn site [Mn^{3+} (0.645 \AA)/ Sb^{5+} (0.60 \AA)/ Mn^{4+} (0.53 \AA), ionic radii are in six-fold coordination] with increase in Sb^{5+} content.

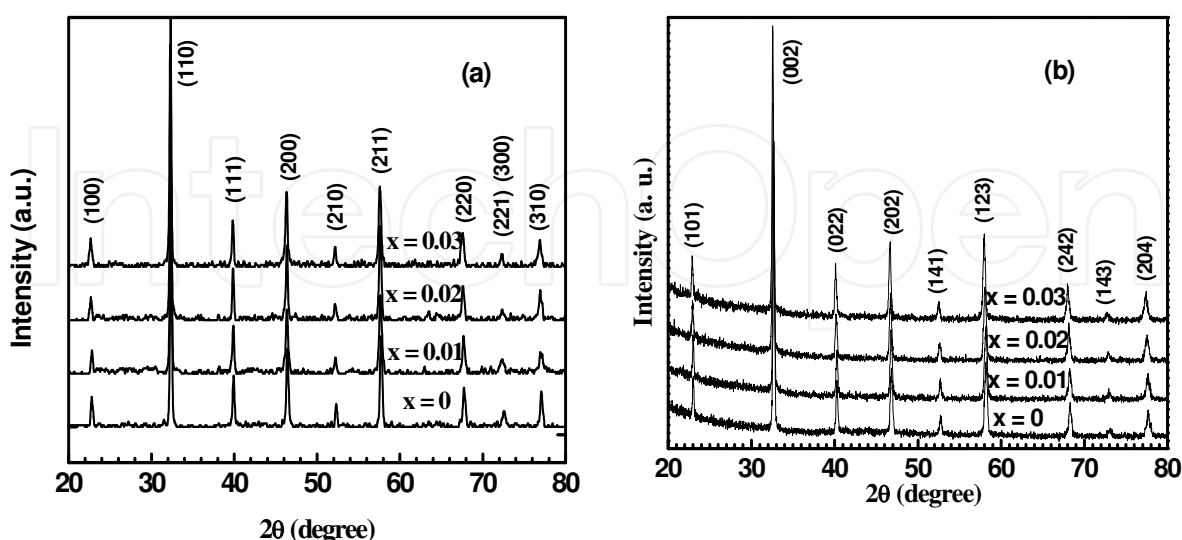


Fig. 4. X-ray diffraction patterns of (a) $\text{La}_{2/3}\text{Ba}_{1/3}(\text{Mn}_{1-x}\text{Sb}_x)\text{O}_3$ and (b) $\text{Pr}_{2/3}\text{Ba}_{1/3}(\text{Mn}_{1-x}\text{Sb}_x)\text{O}_3$ ($0 \leq x \leq 0.03$) samples.

The lattice parameters were calculated using the powder X software. Similar results were also observed in case of Sb-substituted PBMO samples except that the crystal structure here is orthorhombic.

3.2 Morphological studies

The SEM micrographs of bulk LBMO, 3Sb-LBMO, PBMO, 3Sb-PBMO are shown in Fig. 5 (a-d). The SEM micrographs clearly show the grain and grain boundaries. The grains show good connectivity among each other and the grain size is found to increase with doping in both cases. It is assumed that Sb-doping helps in promoting the grain growth.

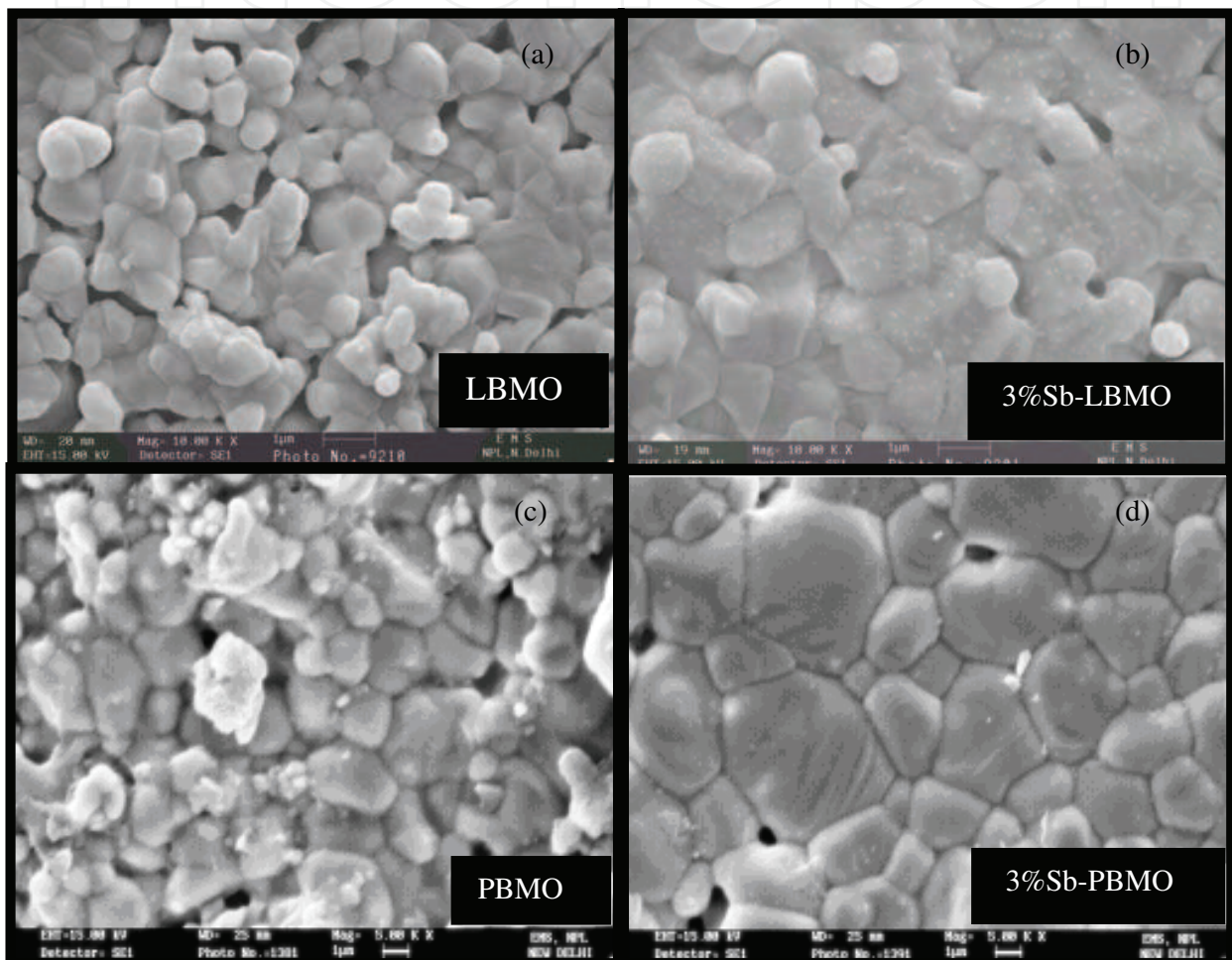


Fig. 5. SEM micrographs of (a) $\text{La}_{2/3}\text{Ba}_{1/3}\text{MnO}_3$, (b) $\text{La}_{2/3}\text{Ba}_{1/3}\text{Mn}_{0.97}\text{Sb}_{0.03}\text{O}_3$ (3Sb-LBMO), (c) $\text{Pr}_{2/3}\text{Ba}_{1/3}\text{MnO}_3$, (d) $\text{Pr}_{2/3}\text{Ba}_{1/3}\text{Mn}_{0.97}\text{Sb}_{0.03}\text{O}_3$ (3Sb-PBMO).

3.3 Electrical resistivity measurement

Figure 6 shows the electrical resistivity variation with temperature (ρ - T) of $\text{La}_{2/3}\text{Ba}_{1/3}(\text{Mn}_{1-x}\text{Sb}_x)\text{O}_3$ and $\text{Pr}_{2/3}\text{Ba}_{1/3}(\text{Mn}_{1-x}\text{Sb}_x)\text{O}_3$ ($0 \leq x \leq 0.03$) samples. Undoped samples LBMO and PBMO exhibit two insulator-metal (I-M) transitions. The higher temperature transition (T_{P1}) is sharp and at $\sim 340\text{ K}$ and 194 K whereas the lower temperature transition (T_{P2}) is broader and at $\sim 250\text{ K}$ and 160 K respectively. In case of LBMO, Ju et al.⁴⁴ reported two transitions at the same temperatures T_{P1} and T_{P2} but the value of the resistivity at T_{P2} in their sample was

lesser than that at T_{P1} but in our case the situation is reverse. The reason for this is the grain size difference in two cases. While the average grain size is $\sim 5 \mu\text{m}$ reported by Ju et al.⁴⁴, it is much smaller ($0.5 \mu\text{m}$) in our case (Fig. 5a). Smaller grain size leads to extra strain at the grain boundary, which eventually leads to the enhancement of the resistivity. However, the same transition temperatures confirm that oxygen content is close to 3.0 in our sample as in the other report Ju et al.⁴⁰ have studied the effect of oxygen variation on the electrical and magnetic properties of LBMO and observed that only the samples having oxygen content close to 3.0 show two transitions in the resistivity-temperature behavior.

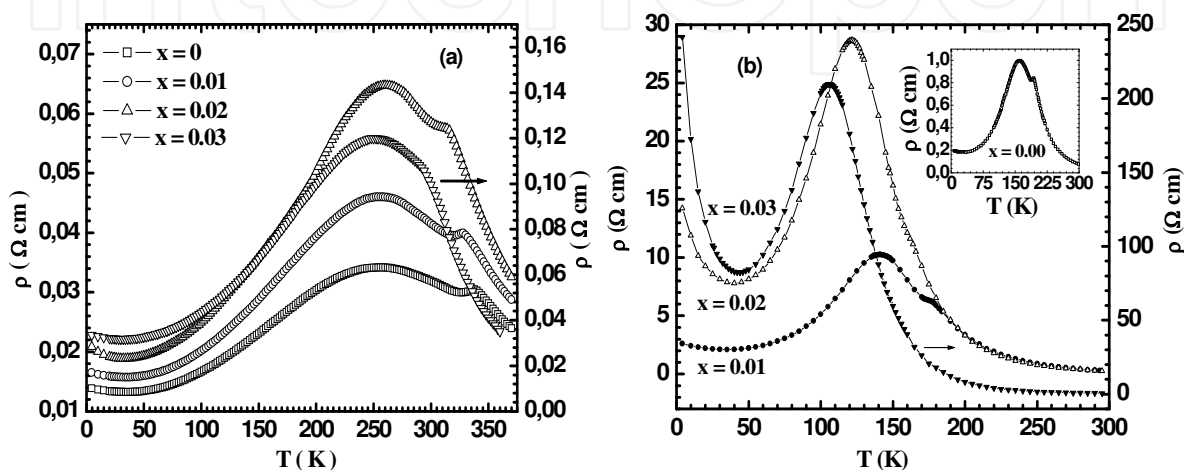


Fig. 6. Electrical resistivity variation with temperature of (a) $\text{La}_{2/3}\text{Ba}_{1/3}(\text{Mn}_{1-x}\text{Sb}_x)\text{O}_3$ and (b) $\text{Pr}_{2/3}\text{Ba}_{1/3}(\text{Mn}_{1-x}\text{Sb}_x)\text{O}_3$ ($0 \leq x \leq 0.03$).

With Sb-doping at the Mn-site the two transitions, in both the cases, shift to lower temperatures successively with the overall increase in the resistivity. However, T_{P1} shifts to lower temperatures at a faster rate than T_{P2} and almost disappear with higher Sb content. T_{P1} is a result of the competition between double-exchange and the super-exchange (SE) mechanisms generally observed in all perovskite manganites. However, T_{P2} results out of the grain boundary effects that in turn arise due to the larger ionic size mismatch between the ions present at the rare-earth site in LBMO and PBMO ($\text{La}^{+3}/\text{Ba}^{+2}$ and $\text{Pr}^{+3}/\text{Ba}^{+2}$ respectively). Due to such ionic size difference the lattice comes under strain but since this is not a situation where the mechanical energy is minimum (which should be the case in equilibrium) and because of the presence of the grain boundaries in the polycrystalline sample, the lattice transfers the extra strain to the grain boundaries to attain a minimum energy configuration. This transferred strain at the grain boundary tilts the MnO_6 octahedra of the LBMO/PBMO lattices present there and thus weakens the electron transfer probability t ($t = t_0 \cos \theta$, which depends upon the angle θ between two neighboring Mn-ions). Therefore the two transitions one from the grain (T_{P1} , where the Mn -ions are more parallel and the electron transfer is easier and hence stronger double exchange mechanism) and the other, T_{P2} , from the grain boundary (weaker double exchange) separate from each other. When Sb^{+5} ion is doped at Mn^{+4} - site, it does not participate in the exchange mechanism between $\text{Mn}^{+3}/\text{Mn}^{+4}$ ions because of its closed shell electronic structure ($4d^{10}$). However, it does decrease the available number of sites where the electron can hop from the

e_g orbital of Mn^{+3} , resulting in some sort of localization of the carriers and the two transitions shift to lower temperatures with increasing of Sb content. It is worthwhile to mention here that ionic size mismatch between the ions present at rare-earth site [Pr^{+3} (1.179Å) and Ba^{+2} (1.47 Å)] in case of PBMO is larger than in LBMO [La^{+3} (1.210Å) and Ba^{+2} (1.47Å)]. Therefore, T_{P2} , is lower in case of PBMO. However, T_{P1} , depends upon the average ionic radius at the rare earth site which is smaller for PBMO that's why T_{P1} is also smaller in this case.

3.4 Electrical resistivity at low temperature (< 50K)

At low temperatures, transport mechanisms such as weak localization^{46,47}, electron-electron interaction^{47,48}, Kondo effect^{49,50,51} etc. can cause an upturn in the resistivity with decreasing temperature, whereas scattering mechanisms such as electron-electron scattering^{52,53}, electron-phonon scattering^{53,54}, electron-magnon scattering^{55,56}, magnon-magnon scattering⁵⁷ increase resistivity with increasing temperature in metals and alloys. Figure 7 shows the temperature dependence of resistivity of Sb-doped LBMO and PBMO systems in the temperature range $4K \leq T \leq 50K$. It is clear that electrical resistivity exhibits an increasing trend with decreasing temperature reminiscent of semiconducting behavior for all compositions. There is a resistivity minimum which is lowest for the undoped samples and shift to high temperatures with antimony substitution. In order to analyze the electrical resistivity behavior at low temperatures we tried to fit the data using the following equation:

$$\rho(T) = \rho_0 - \rho_1 T^{1/2} + \rho_2 T^2 + \rho_5 T^5 \quad (3)$$

where $\rho_0 = 1/a$ and $\rho_1 = b/a^2$ are constants. 'a' is temperature independent residual conductivity; 'b' is the diffusion constant and is due to weak localization effect⁴⁶. The other two terms viz. $\rho_2 T^2$ and $\rho_5 T^5$ arise due to the electron-electron and electron-phonon scattering⁵³. The fitting parameters $\rho_0, \rho_1, \rho_2, \rho_5$ for the two systems are shown in Table 1.

La _{2/3} Ba _{1/3} (Mn _{1-x} Sb _x)O ₃ (0 ≤ x ≤ 0.03)				
Sample	ρ_0 (Ω cm)	ρ_1 (Ω cm K ^{-1/2})	ρ_2 (Ω cm K ⁻²)	ρ_5 (Ω cm K ⁻⁵)
x = 0	0.01436	0.00023	1.8885×10 ⁻⁷	6.89×10 ⁻¹³
x = 0.01	0.01723	0.00033	3.3297×10 ⁻⁷	6.9613×10 ⁻¹³
x = 0.02	0.02282	0.00093	1.269×10 ⁻⁶	3.184×10 ⁻¹³
x = 0.03	0.03529	0.00081	9.8659×10 ⁻⁷	1.8152×10 ⁻¹²
Pr _{2/3} Ba _{1/3} (Mn _{1-x} Sb _x)O ₃ (0 ≤ x ≤ 0.03)				
x = 0	0.2175	0.0082	8.9×10 ⁻⁶	4.83×10 ⁻¹¹
x = 0.01	3.0015	0.1922	1.7×10 ⁻⁴	5.26×10 ⁻¹⁰
x = 0.02	19.044	2.4068	2.53×10 ⁻³	7.18×10 ⁻¹⁰
x = 0.03	362.885	61.8983	7.69×10 ⁻²	1.09×10 ⁻⁷

Table 1. Various fitting parameters for (La/Pr)_{2/3}Ba_{1/3}(Mn_{1-x}Sb_x)O₃ (0 ≤ x ≤ 0.03) systems using equation (3).

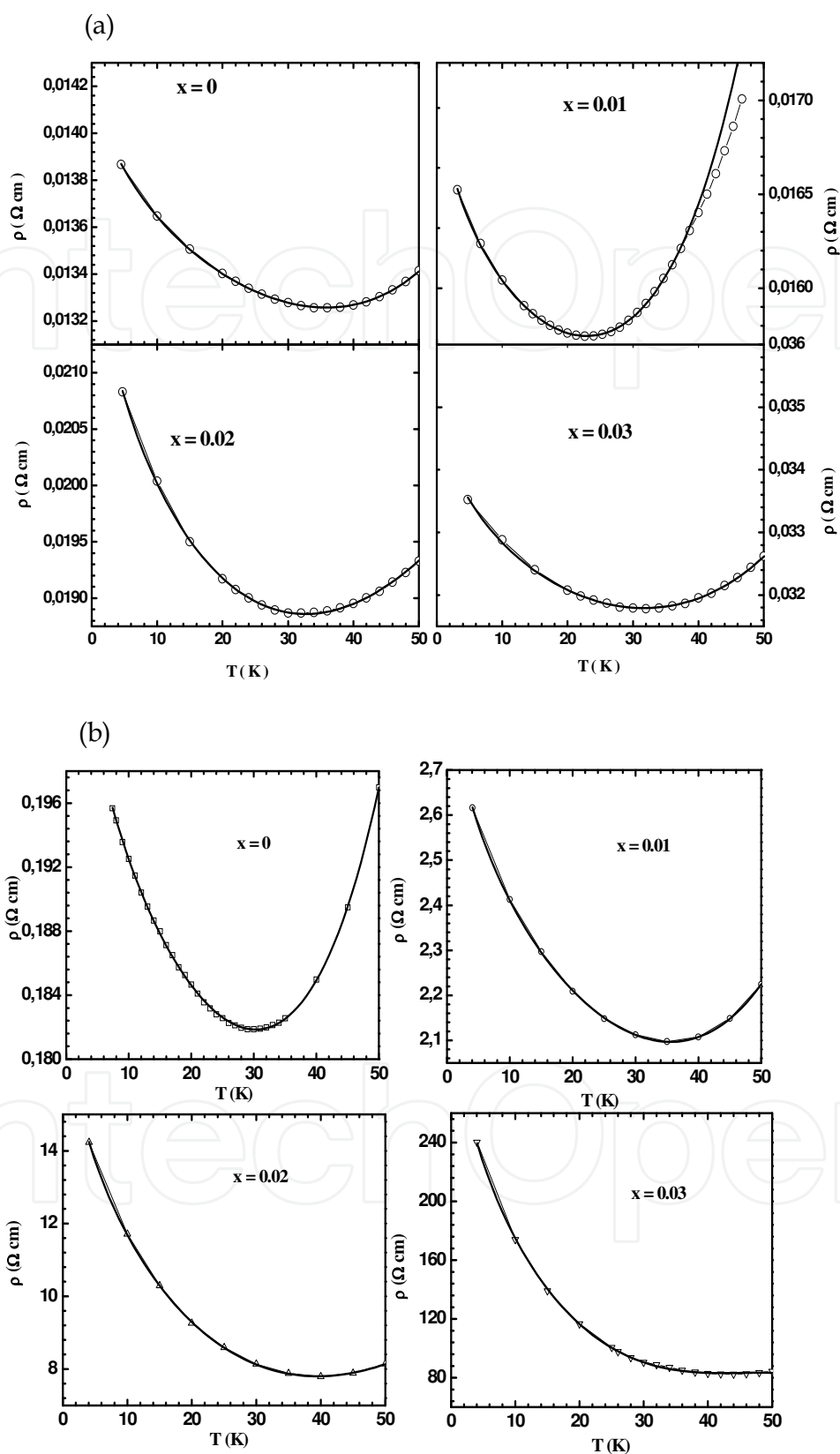


Fig. 7. Electrical resistivity variation with temperature below 50K (a) $La_{2/3}Ba_{1/3}(Mn_{1-x}Sb_x)O_3$ and, (b) $Pr_{2/3}Ba_{1/3}(Mn_{1-x}Sb_x)O_3$ ($0 \leq x \leq 0.03$). Solid line shows the fitting with the Eq. (3).

It is observed that the value of fitting parameters ρ_0 , ρ_1 , ρ_2 , ρ_5 increases with doping. This indicates that the weak localization, electron-electron and electron-phonon scattering increases with doping and making pristine material more disordered. This is also obvious from the fact that random distribution of ions $\text{La}^{+3}/\text{Pr}^{+3}/\text{Ba}^{+2}/\text{Mn}^{+3}/\text{Mn}^{+4}/\text{Sb}^{+5}$ leads to random variation in the potential experienced by the electrons so the electrons get trapped due to less kinetic energy at low temperatures. The other two terms i.e. electron-electron and electron-phonon scattering will increase because of the difference in ionic sizes. It is worth mentioning here that in addition to these effects the Coulomb blockade (CB) effect⁵⁸ could also contribute to the observed electrical resistivity upturn as the large ionic size mismatch between $\text{La}^{+3}/\text{Pr}^{+3}$ and Ba^{+2} ions leads to the strong disorder at the grain boundaries and eventually increases the Coulomb charging energy E_C leading to increase in resistivity. This would get further enhanced for grains with smaller sizes ($E_C \propto 1/d$). In this case grain size d , however, has increased with Sb-doping (figure 5), which implies that E_C should decrease and hence the resistivity upturn should also decrease but here a reverse situation is observed. The CB effect, therefore, cannot account for the resistivity upturn for the Sb-doped samples, even though it might be one of the possible sources of localization in the pristine sample case.

3.5 Transport mechanism in the metallic region

We used the following Eq. to fit the metallic region of the temperature dependent electrical resistivity data

$$\rho = \rho_0 + \rho_{2.5}T^{2.5} \quad (4)$$

here ρ_0 is the temperature independent residual resistivity. $\rho_{2.5}T^{2.5}$ represents the electrical resistivity due to electron-magnon scattering processes in the ferromagnetic phase. We found that in the metallic regime electrical resistivity data for Sb doped samples best fit the Eq. (4). The quality of these fittings, in general, is evaluated by comparing the square of the linear correlation coefficient (R^2) obtained for each equation. The values of R^2 were found as high as 99.9% for Eqn. (4) which confirms the applicability of electron-magnon scattering process. The obtained fitted parameters are given in Table 2. It is observed that value of both ρ_0 and $\rho_{2.5}$ increases with doping. This reflects the dominating nature of the electron-magnon scattering mechanism with increasing Sb content. Similar results were observed for the Sb-doped PBMO manganites.

Sample	ρ_0 (Ω cm)	$\rho_{2.5}$ (Ω cmK ^{-2.5})	R^2
x = 0	0.11296	8.1315x10 ⁻⁶	0.99994
x = 0.01	0.31814	0.00005	0.99905
x = 0.02	3.18173	0.00015	0.99962
x = 0.03	33.90211	0.00103	0.99952

Table 2. Fitting parameters obtained using Eq. (4) after fitting the metallic region of $\text{La}_{2/3}\text{Ba}_{1/3}(\text{Mn}_{1-x}\text{Sb}_x)\text{O}_3$ ($0 \leq x \leq 0.03$) system.

3.6 Transport mechanism above T_{P1}

Conduction in manganites at higher temperature ($T \geq T_p$) is governed either by variable range hopping (VRH) or by small polaron hopping (SPH) depending on the Debye temperature (θ_D)^{59,60}. If $T > \theta_D/2$, the conduction mechanism is governed by small polarons and these polaronic models can be either adiabatic or non-adiabatic. Since the Debye temperature of the LBMO system is ~ 400 K⁶¹ so the polaronic model can be applied to the insulating region above T_{P1} . The adiabatic small polaron hopping model is given by^{59,60}:

$$\rho = \rho_0 T \exp(E_p/k_B T) \quad (4)$$

where ρ_0 is the residual electrical resistivity, E_p is the activation energy and k_B is the Boltzmann's constant. We estimated the activation energy E_p and it is found to increase with Sb content as shown in Table 3. Similar results were observed for Sb-doped PBMO system.

Sample	E_p (meV)	E_S (meV)	α	W_H (meV)	E_p (meV)
x = 0	91.2	21.693	-0.8491	69.507	139.014
x = 0.01	98.02	14.016	-0.6444	84.004	168.008
x = 0.02	112.92	7.903	-0.457	105.001	210.002
x = 0.03	126.15	5.869	-0.3941	120.281	240.562

Table 3. Activation energies E_p (from electrical resistivity) and E_S (from Thermoelectric Power), $W_H (= E_p - E_S)$ corresponds to polaron binding energies for Sb-doped LBMO series.

3.7 Magnetoresistance studies

Generally, application of the external magnetic field enhances spin ordering, promotes the charge transfer and thus suppresses the electrical resistivity. Alignment of the spins of the neighboring Mn-sites favors the electronic motion. Figure 8 (a) & (b) shows the temperature dependent magnetoresistance behavior of all the samples from 77K to 300K, for an applied magnetic field of 0.6T. For Sb-doped LBMO samples a sharp peak is observed in all the samples near T_{P1} and below it MR increases continuously reflecting the important role of grain boundaries in producing LFMR (in case of single crystals MR decreases very fast below T_{P1}). With Sb doping the MR is found to increase. Magnetoresistance for 3% Sb-doped sample $\text{La}_{2/3}\text{Ba}_{1/3}\text{Mn}_{0.97}\text{Sb}_{0.03}\text{O}_3$ is 6% under the application of 0.6 T magnetic field which shows that this material may be useful from the application point of view. In case of Sb-doped PBMO (Fig. 8b), $\text{Pr}_{2/3}\text{Ba}_{1/3}(\text{Mn}_{1-x}\text{Sb}_x)\text{O}_3$ series, besides a usual peak near T_{P1} there is the development of an additional peak with increasing Sb-content. For 3% Sb sample low temperature peak MR is larger than that the high temperature peak. Also, in case of Sb-doped PBMO, MR value at the respective T_{P1} decreases with Sb which is reverse to that of Sb-LBMO system. The difference of MR below T_{P1} may be attributed to the varying grain boundary effects in both the cases. To identify this we carried out the MR measurement with magnetic field variation at 77K and the results are shown in figure 9 (a) & (b). MR behavior of Sb-doped LBMO series exhibits the trend of spin polarized tunneling proposed by Hwang et al.⁶² with lower applied field MR increases sharply and at higher values of the field it gets saturated. Whereas in case of Sb-doped PBMO, it seems that spin dependent scattering and not the spin polarized tunneling dominates the process.

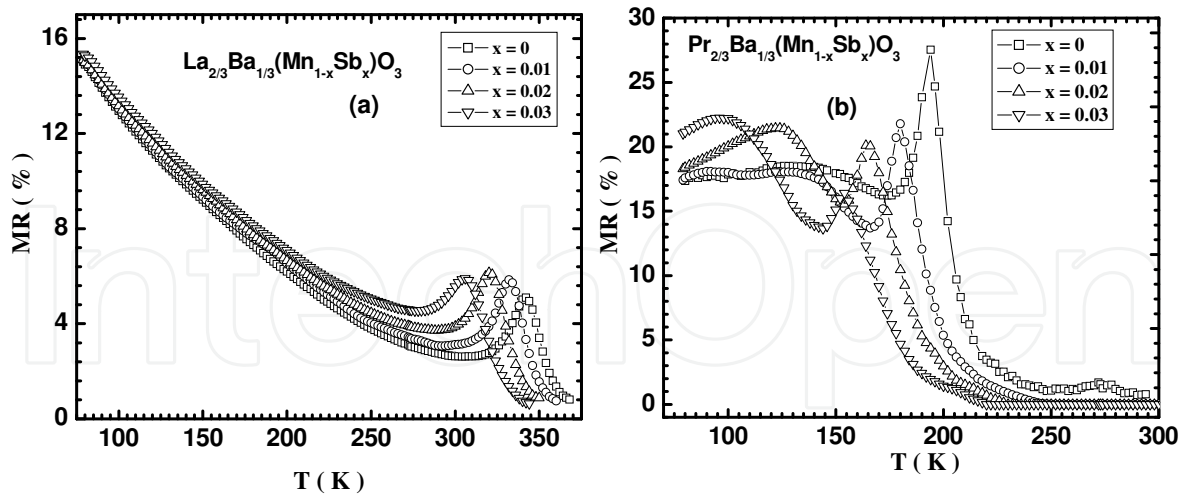


Fig. 8. Magnetoconductance variation with temperature of Sb-LBMO and Sb-PBMO samples under 0.6 T magnetic field.

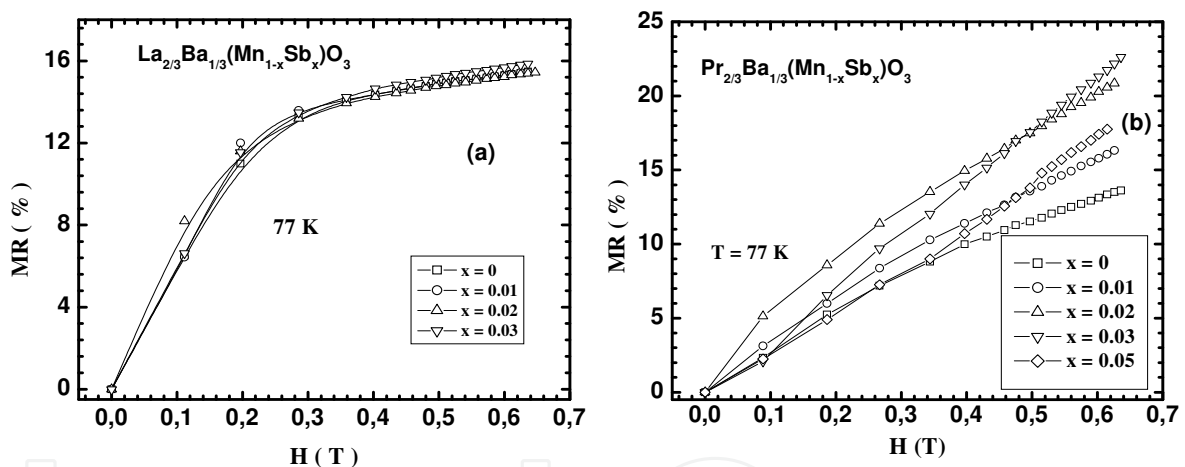


Fig. 9. Magnetoconductance variation with magnetic field of Sb-LBMO and Sb-PBMO samples at 77K.

3.8 Thermoelectric power

Thermoelectric Power (TEP) is especially suited to explore the carrier dynamics because it is expected to be very sensitive to the local moments⁶³ and thus it monitors the ferromagnetic transition and provide new insight into the dynamics of manganite systems. $S(T)$ is less affected by the presence of grain boundaries and hence the grain boundary effects that are observed in the resistivity temperature measurements, can be masked. The thermoelectric power data for the two series is shown in Figure 10. In the case of Sb-doped LBMO series, a crossover of thermopower is observed from positive to negative at temperature $T^* = 264, 258, 250, 241$ and 210 K respectively with increasing Sb-content whereas in Sb-PBMO series only two samples *viz.* pristine PBMO and 1% Sb-doped exhibit such behavior. Further, in

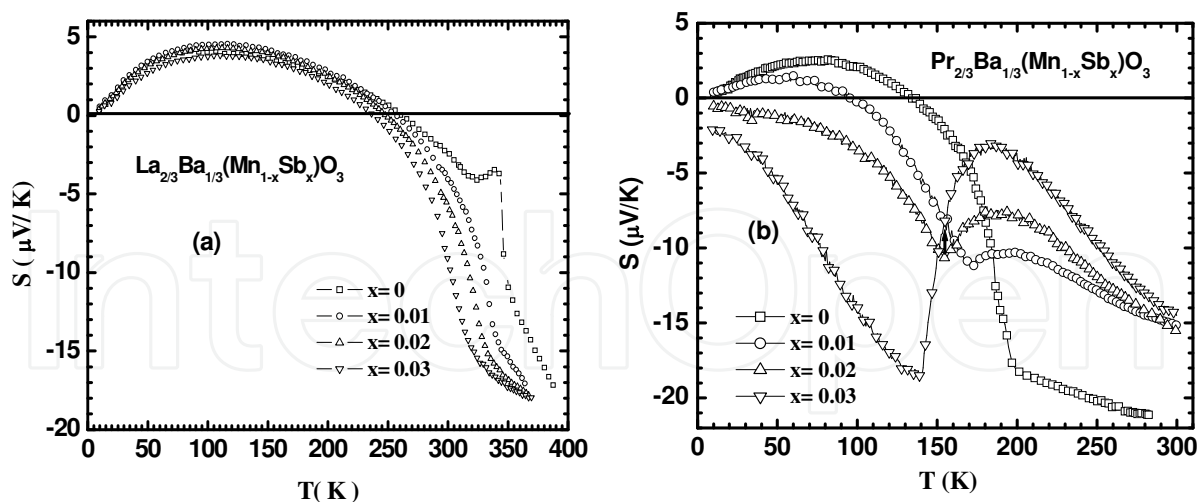


Fig. 10. Thermopower variation with temperature of Sb-LBMO and Sb-PBMO samples.

case of Sb-LBMO, insulator-metal transition T_S is very close to T_{PI} for all the samples whereas for Sb-PBMO, the two transitions are closer for PBMO sample only and as the doping of Sb increases at Mn-site a peak starts developing near the phase transition and separation between T_{PI} and T_S increases. The development of the thermopower peak and separation of T_{PI} and T_S can be related to the increase in magnetic inhomogeneity due to increase in spin entropy by the weakening of double exchange interaction between $\text{Mn}^{3+}/\text{Mn}^{4+}$ ions in the sample with Sb-doping that could lead to a phase separation. In the ferromagnetic state, the magnitude of the observed thermoelectric power in the range of a few $\mu\text{V}/\text{K}$ seems to be reminiscent of the metallic system. In order to explain the change of sign of thermopower from hole-like behavior (positive) to electron-like behavior (negative) in the metallic ferromagnetic (FMM) state we adopt the model given by Asamitsu et al.⁶⁴ that is based on the vanishing of the exchange interaction J . This interaction arises due to the excitation of the electrons from the valence band (VB) t_{2g} to the conduction band (CB) e_g . The mobility of electrons in the conduction band is high, leading to a negative thermopower. The degeneracy of the e_g band seems to be gradually lifted as the temperature is lowered below T^* and the thermopower changes its sign from negative to positive with the increase of spin polarization. Based on thermoelectric data, we have attempted to explore various mechanisms governing the thermoelectric power in different temperature regions. It would be worthwhile mentioning here that the effect of Jahn-Teller distortion in manganites results in strong electron-phonon coupling and hence the formation of polarons⁶⁵. Therefore, charge carriers in the insulating region above T_P are not itinerant and transport properties are governed by thermally activated carriers (polarons)⁶⁶. We, therefore, fitted the $S(T)$ data above T_S (T_{PI}) fig. 10, with the Mott's polaron hopping relation⁶⁶:

$$S = k_B/e [(E_S/k_B T) + a] \quad (5)$$

where e is the electronic charge; k_B is the Boltzmann constant, E_S is the activation energy required to activate the hopping of the carriers and a is a constant related to the kinetic energy of the polarons⁶⁷. The value of $a < 1$ suggests the conduction due to small polarons

hopping (SPH) whereas $a > 2$ corresponds to the case of large polaron hopping (LPH)⁶⁶. The fitting for two systems are shown in figure 11. The electrical resistivity activation energy E_ρ and the thermopower activation energy E_S , are shown in Table 3 for Sb-doped LBMO manganites and from there it is clear that E_ρ is much larger than E_S . Such a large difference in the values of two activation energies is the indication of the applicability of the small polaron-hopping (SPH) model in the insulating region above T_{P1} which is further corroborated by the value of constant a (less than 1). In the framework of SPH model, E_ρ is the sum of the activation energy required for the creation of the carriers and activating the hopping of the carriers and E_S is the energy required to activate the hopping of carriers only. Hence E_S is much smaller than E_ρ . Based on E_ρ & E_S , both the polaronic energy $W_H = E_\rho - E_S$ and the polaronic formation energy $E_P = 2W_H$ are also given in Table 3 for Sb substituted LBMO.

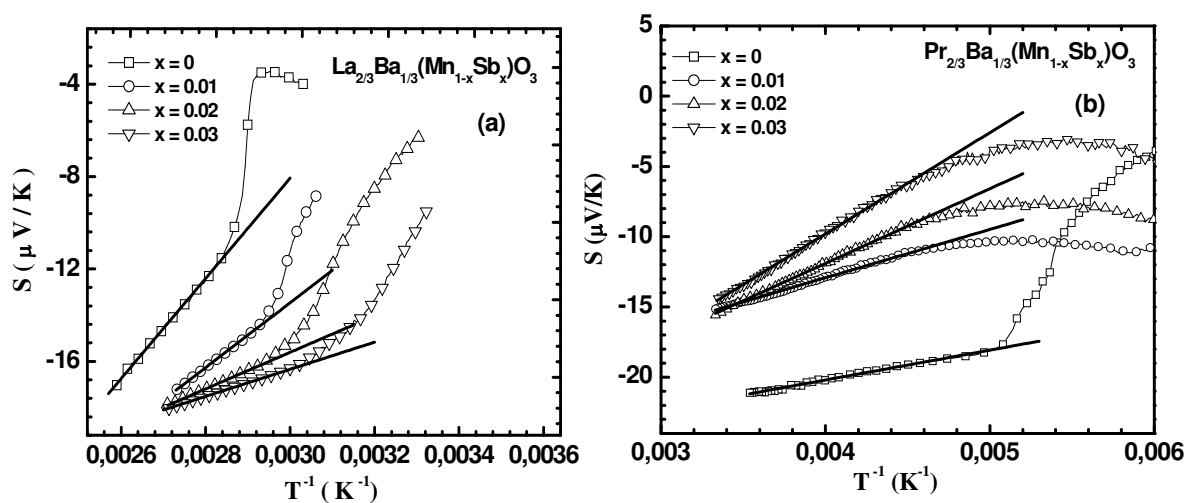


Fig. 11. Thermopower fitting above T_S of Sb-LBMO and Sb-PBMO samples using Eq. (5).

Similar to $\rho(T)$ data, several factors, such as impurity, complicated band structure, electron-electron, electron-magnon scattering etc also affect $S(T)$ data in the FM metallic regime. $S(T)$ data in this intermediate temperature FM metallic region has been analyzed by the following relation^{68,69}:

$$S = S_0 + S_{3/2}T^{3/2} + S_4T^4 \quad (6)$$

here S_0 , $S_{3/2}$, and S_4 are fitting parameters. S_0 has no physical origin but inserted to account for the low temperature data, $S_{3/2}T^{3/2}$ is attributed to single magnon scattering process^{68,70}. The term S_4T^4 dominant in high temperature region near T_C , is thought to arise from spin wave fluctuation in the FM phase^{68,70}. Figure 12 shows the fitting of Eq. (6) in the metallic region of the Sb-doped LBMO samples and the fitting parameters are given in Table 4. From Table 4, it is clear that $S_{3/2}$ is nearly five orders of magnitude larger than that of S_4 , implying that the second term i.e. electron-magnon scattering in Eq.(6) dominates the transport mechanism in the FM metallic regime below T_{P1} . The hole-like to electron-like cross over in thermoelectric power arises due to the fact that $S_4 < 0$. Then due to higher power of T , the term S_4T^4 will dominate for large T making thermopower negative. Hence, based on the electrical resistivity and thermopower data fittings we can conclude that insulating region

above T_{PI} is governed by the small polaron hopping (SPH) model whereas electron-magnon scattering is dominant in ferromagnetic metallic region.

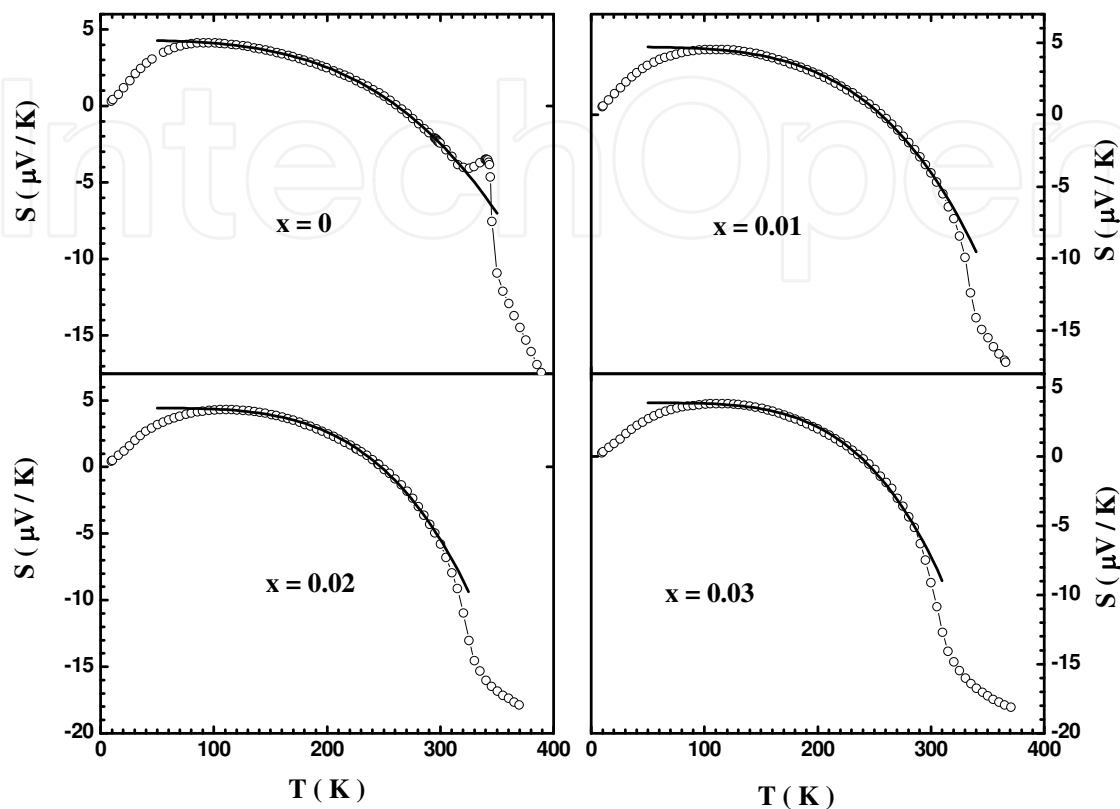


Fig. 12. Thermopower fitting of $\text{La}_{2/3}\text{Ba}_{1/3}(\text{Mn}_{1-x}\text{Sb}_x)\text{O}_3$ ($0 \leq x \leq 0.03$). Solid line represents the fitting with Eq. (6).

Sample	S_0 ($\mu\text{V}/\text{K}$)	$S_{3/2}$ ($\mu\text{V}/\text{K}^{2.5}$)	S_4 ($\mu\text{V}/\text{K}^5$)
$x = 0$	4.5365 ± 0.03756	-0.00036 ± 0.00002	$-6.3773 \times 10^{-10} \pm 9.951 \times 10^{-12}$
$x = 0.01$	4.7905 ± 0.06958	-0.00009 ± 0.00004	$-1.0287 \times 10^{-9} \pm 2.2475 \times 10^{-11}$
$x = 0.02$	4.43458 ± 0.08659	0.00003 ± 0.00006	$-1.212 \times 10^{-9} \pm 3.5867 \times 10^{-11}$
$x = 0.03$	3.69632 ± 0.0923	0.00028 ± 0.00006	$-1.4882 \times 10^{-9} \pm 3.8002 \times 10^{-11}$

Table 4. Electron-magnon fitting parameters of thermoelectric power of Sb-LBMO series in the FM region with Eq. (6).

3.9 Thermal conductivity

Figure 13 shows the temperature dependent thermal conductivity (κ) measurements of Sb-doped manganites. The magnitude of $\kappa(T)$, typically of non-crystalline materials (bad metals), lies in the range of 5-70 mW/cm K. For a crystalline solid, such a low value of thermal conductivity in manganites can be attributed to the disorder due to strong Jahn-Teller effect. Magnitude of κ decreases with decreasing temperature down to T_κ (close to T_S and T_{PI}), which is unusual since the high temperature thermal conductivity of the crystalline insulators is mostly a decreasing function of temperature and cannot be attributed to high temperature electron or phonon processes. Also the thermal conductivity decreases with Sb-doping in the whole temperature range. As discussed earlier, number of Mn^{+3} -ions increases with Sb-doping and since Mn^{+3} is a Jahn-Teller ion it causes the distortion in $Mn^{+3}O_6$ octahedra which eventually scatters the phonons and causes κ to decrease with Sb-doping.

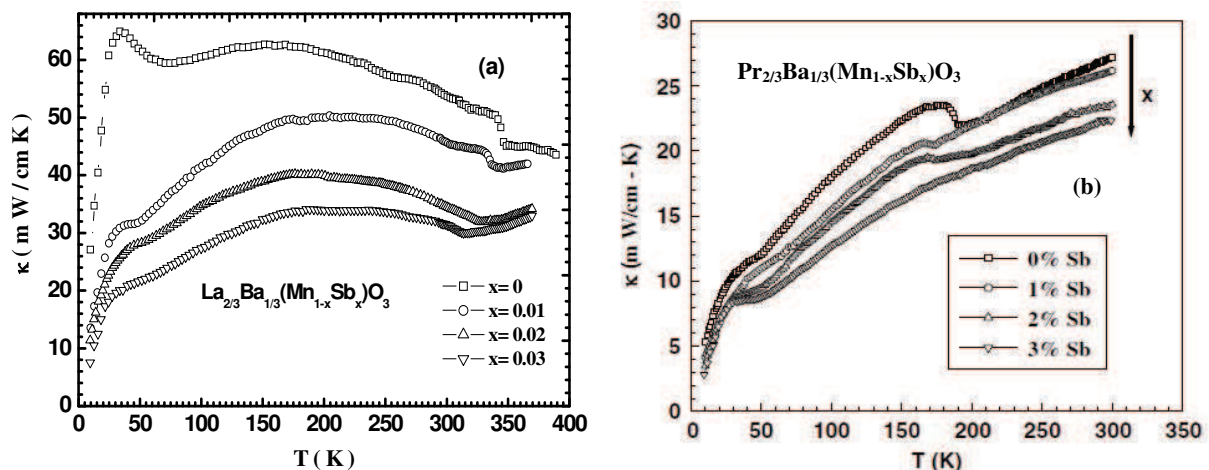


Fig. 13. $\kappa(T)$ variation of Sb-LBMO and Sb-PBMO samples.

At high temperatures thermal conductivity of the crystalline solids is expected to follow the temperature dependency according to the formula $\kappa \propto aMC_p\theta_D/\gamma^2T$, where a is the lattice constant, M is the mass per atom, C_p is the specific heat, θ_D is the Debye temperature, and γ is the Gruneisen constant with a value ranging from 2-3 for solids. These parameters are considered to be a weak function of temperature at high temperatures. As a result, κ is expected to increase with decreasing temperature. However, in the present case κ decreases monotonically with temperature for all the samples, which is peculiar. Neutron scattering experiments in these manganites, however, have shown that the Gruneisen constant γ is much higher (~ 180) than usual and decreases remarkably with temperature⁷¹. Thus, high temperature behaviour of κ in the paramagnetic state could be understood in terms of the local anharmonic lattice distortions associated with small polarons⁷². An anomaly in thermal conductivity below T_{PI} has been observed for all the studied samples. It may be noticed that this anomaly is closely related to the phase transition at T_{PI} . Below T_{PI} , κ first increases for pure and 1% doped samples and change in slope for the other doped samples which may be attributed to the reduction in phonon-phonon scattering (Umklapp process) as a result of JT distortions which become delocalized alongwith the charge carriers. The small peak observed in thermal conductivity below 35K in all the samples is an indication of the

crossover from Umklapp to defect limited scattering^{73,74}. In general, the total thermal conductivity for ordinary metals and semimetals is sum of the electronic and lattice terms. The electronic thermal conductivity κ_e can be evaluated using Wiedemann-Franz (W-F) law $\kappa_e \rho/T=L$. Here ρ is the electrical resistivity and the Lorentz number L is $2.45 \times 10^{-8} \text{ W}\Omega/\text{K}^2$. Therefore, using the above W-F formula electronic thermal conductivity at any particular temperature (say 250K, where the value of electrical resistivity is shown in Table 5), is very small to the total thermal conductivity κ at that temperature. Hence the measured κ is suggested to arise from phonons, the contribution of charge carriers being negligible.

Sample	$\rho_{250\text{K}}$ ($\text{m}\Omega\text{-cm}$)	κ_e ($\text{mW}/\text{cm-K}$)	ΔS (in R)	ΔC_{mag} (J/mol-K)
$x = 0$	30.48	0.201	0.0917	12.065
$x = 0.01$	45.95	0.1333	0.194	17.45
$x = 0.02$	64.2	0.0954	0.1265	12.71
$x = 0.03$	119.97	0.0511	0.1231	10.116

Table 5. Electronic thermal conductivity, entropy and magnon contribution to the specific heat for Sb-doped LBMO series.

3.10 Specific heat

The observed specific heat measurements [$C_p(T)$] carried out from 85 K to 380 K for the Sb-doped manganites is shown in Figure 14. It increases with temperature for all pure as well as doped samples. There is not much effect of Sb doping up to $\sim 250\text{K}$. However all the samples show a peak in its $C_p(T)$ plot just below the corresponding paramagnetic-ferromagnetic transition temperature (T_C). For clarity, each curve has been offset by 10 J/mole K. The transition temperature, defined as the peak position, being lower than the

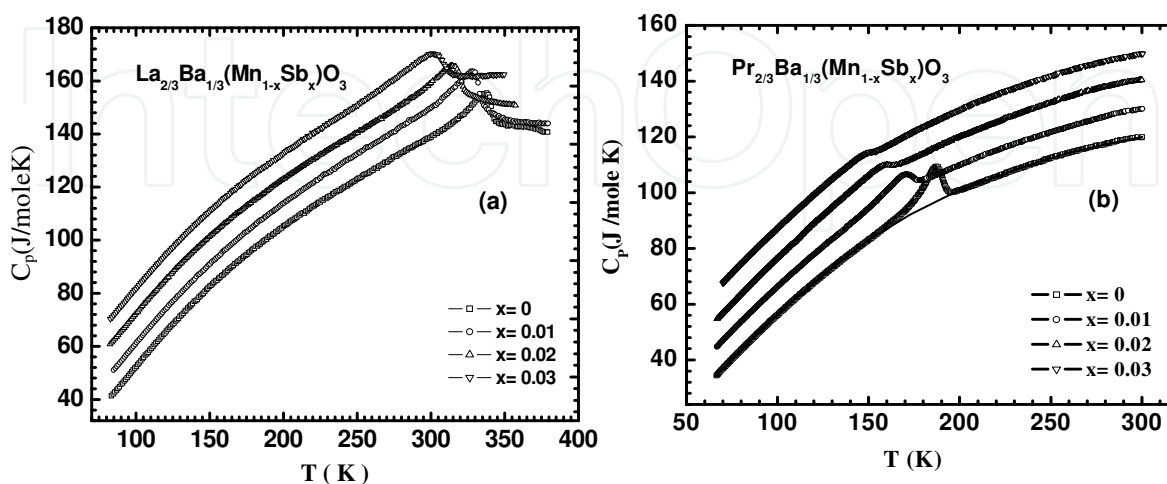


Fig. 14. C_p variation with temperature of Sb-LBMO and Sb-PBMO samples.

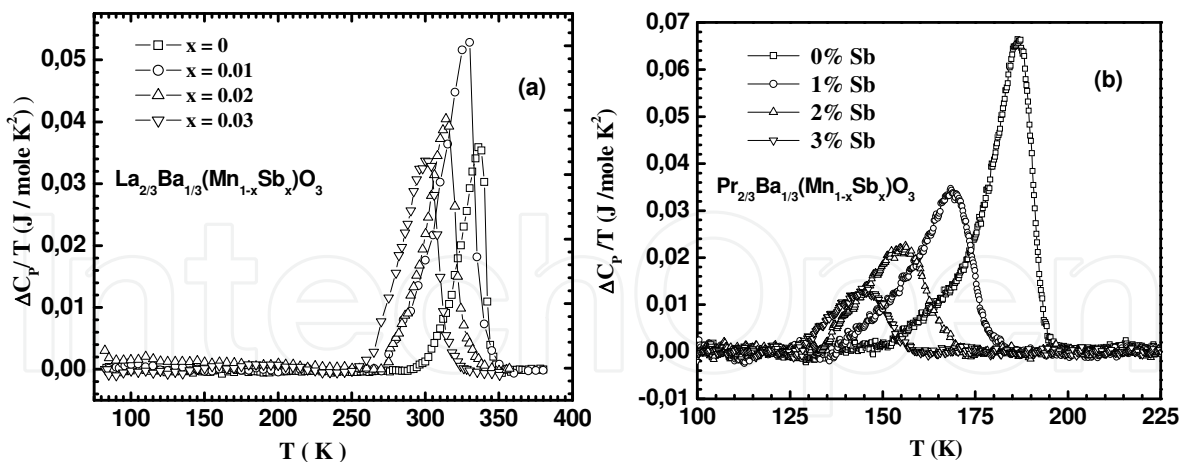


Fig. 15. Specific heat jumps with background subtracted for Sb-LBMO and Sb-PBMO samples.

corresponding I-M transition temperature T_{P1} reflects that the specific heat anomaly is related to the magnetic ordering in the sample due to paramagnetic-ferromagnetic transition. This specific heat anomaly shifts to lower temperatures and becomes progressively broader with Sb-doping. However, no such anomaly corresponding to T_{P2} could be observed in our measurements, which again confirm that thermal measurements are insensitive to the grain boundaries. Considerable broadening in the $C_p(T)$ curves with Sb substituted samples implies the increase in local structural disordering or/and magnetic inhomogeneity.

In order to separate the lattice contribution and to estimate the excess specific heat (ΔC_p) due to magnetic ordering a smooth background line (tangential to both end points and shown in Fig.14(b) for pristine PBMO manganite) was subtracted from the data of every sample and the obtained curves are plotted in Figure 15. Integration of $\Delta C_p/T$ gives the excess entropy (ΔS) under the C_p anomaly of the specific heat curve. Considerable reduction in the value of ΔS is observed with the increase in Sb content (Table 5). This confirms that magnetic inhomogeneity increases with Sb. The value of ΔS is also less than the theoretical value $R \ln 2$ for a paramagnetic-ferromagnetic transition (where R is the ideal gas constant). This discrepancy can be attributed to the magnetic inhomogeneity or partially canted spins in the ferromagnetic state.

4. Conclusions

Substitution effect of Sb^{5+} ion on the structural, morphological, magneto-transport and thermal properties (including thermoelectric power, specific heat and thermal conductivity) of $La_{2/3}Ba_{1/3}MnO_3$ (LBMO) and $Pr_{2/3}Ba_{1/3}MnO_3$ (PBMO) manganites have been carried out. Structural measurements on polycrystalline samples synthesized showed that lattice parameters increase with Sb-doping. The grain size is also found to increase with Sb. Electrical resistivity variation with temperature of these manganites showed two insulator-metal like transitions (T_{P1} and T_{P2}) which suppressed to low temperatures with an overall increase in electrical resistivity with Sb substitution. Thermal measurements and their

analyses show that high temperature insulating region was governed by the hopping of small polarons and the metallic region below T_{PI} was dominated by electron-magnon scattering process. Intrinsic magneto-resistance (MR due to grain) at T_{PI} (high temperature insulator-metal transition) was suppressed whereas extrinsic MR (due to grain boundary) got enhanced with Sb. While in the case of Sb-LBMO, MR kept on increasing below a peak near T_{PI} in all samples whereas in Sb-PBMO system second peak appeared in MR with its value larger than that at the high temperature peak. MR ~7% was observed in 3% Sb-LBMO sample at room temperature under 0.6T magnetic field which indicates the potential application of these materials as low magnetic field sensors.

5. Acknowledgement

The authors are thankful to Prof. Y. K. Kuo (National Dong Hwa University Taiwan), Prof. G. L. Bhalla (University of Delhi, India), Prof. Ashok Rao (Manipal University, India) and Prof. D. K. Pandya (I.I.T. Delhi, India) for scientific discussions. One of the authors (SKA) would like to thank the Council of Scientific and Industrial Research (CSIR, India) for providing the financial grants under the Emeritus Scientist Scheme.

6. References

- [1] W. Thomson, Proc. Roy. Soc. Lond. 8 (1857) 546.
- [2] F. Y. Yang, K. Liu, D. H. Reich, P. C. Searson and C. L. Chien, Science 284 (1999) 1335.
- [3] K. Chahara, T. Ohno, M. Kasai and Y. Kozono, Appl. Phys. Lett. 63 (1993) 1990.
- [4] R. von Helmolt, J. Wocker, B. Holzapfel, M. Schultz and K. Samver, Phys. Rev. Lett. 71 (1993) 2331.
- [5] S. Jin, T. H. Tiefel, M. McCormack, R. A. Fastnacht, R. Ramesh and L. H. Chen, Science 264 (1994) 413.
- [6] G. C. Xiong, Q. Li, H. L. Ju, S. M. Bhagat, S. E. Lofland, R. L. Greene, and T. Venkatesan, Appl. Phys. Lett. 67 (1995) 3031.
- [7] C. W. Searle and S. T. Wang, Can. J. Phys. 47 (1969) 2703.
- [8] C. W. Searle and S. T. Wang, Can. J. Phys. 48 (1970) 2023.
- [9] R. M. Kusters, D. A. Singleton, D. A. Keen, R. AcGreevy and W. Hayes, Physica B 115 (1989) 362.
- [10] S. S. P. Parkin, Annu. Rev. Mater. Sci. 25 (1995) 357.
- [11] H. L. Ju, C. Kwon, Q. Li, R. L. Green and T. Venkatesan, Appl. Phys. Lett. 65 (1994) 2108.
- [12] Y. G. Zhao, M. Rajeswari, R. C. Srivastva, A. Biswas, S. B. Ogale, D. J. Kang, W. Prellier, Z. Chen, R. L. Green and T. Venkatesan, J. Appl. Phys. 86 (1999) 6327.
- [13] W. Prellier, A. M. Haghiri-Gosnet, B. Mercey, P. Lecoer, M. Hervieu, C. Simon and B. Raveau, Appl. Phys. Lett. 77 (2000) 1023.
- [14] P. A. Cox, "Transition Metal Oxides: An Introduction to their Electronic Structure and Properties", Clarendon Press, Oxford (1995).
- [15] W. E. Pickett and D. J. Singh, Phys. Rev. B. 53 (1995) 1146.
- [16] H. A. Jahn and E. Teller, Proc. Roy. Soc. London. Series A, Mathematical and Physical Sciences (1943-1990), 161 (1937) 220.

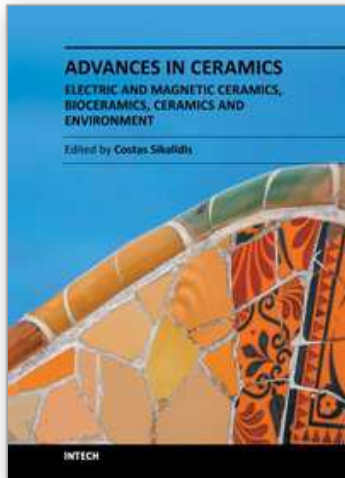
- [17] R. Orbach and H. J. Stapleton, *Electron Spin-Lattice Relaxation*, Chapter 2 of “*Electron Paramagnetic Resonance*” Ed. S. Geschwind (Plenum Press, New York, 1972).
- [18] J. Kanamori, *J. Appl. Phys. (Suppl.)* 31 (1960) 14S.
- [19] Y. Tokura (Ed.), *Colossal Magnetoresistive Oxides*, (Gordon and Breach, London, U. K., 2000).
- [20] A. J. Millis, B. I. Shraiman and R. Mueller, *Phys. Rev. Lett.* 77 (1996) 175.
- [21] K. H. Ahn, X. W. Wu, K. Liu, C. L. Chien, *J. Appl. Phys.* 81 (1997) 5505.
- [22] J. W. Cai, C. Wang, B.-G. Shen, J.-G. Zhao, W.-S. Zhan, *Appl. Phys. Lett.* 71 (1997) 1727.
- [23] J. Blasco, J. Garcia, J.M. de Teresa, M.R. Ibarra, J. Perez, P.A. Algarabel, C. Ritter, *Phys. Rev. B* 55 (1997) 8905.
- [24] Y. Sun, X. Xu, L. Zheng, Y. Zhang, *Phys. Rev. B* 60 (1999) 12317.
- [25] E. Sotirova, X. L. Wang, J. Horvat, T. Silver, K. Konstantinov, H. K. Liu, *Supercond. Sci. Tech.* 15 (2002) 346.
- [26] J. Yang, W. H. Song, Y. Q. Ma, R. L. Zhang, B. C. Zhao, Z. C. Sheng, G. H. Zheng, J. M. Dai, Y. P. Sun, *Phys. Rev. B* 70 (2004) 092504.
- [27] S. Pal, E. Bose, B. K. Chaudhuri, H. D. Yang, S. Neeleshwar and Y. Y. Chen, *J. Magn. Mag. Mater.* 293 (2005) 872.
- [28] R. Ang, Y. P. Sun, J. Yang, X. B. Zhu and W. H. Song, *J. Appl. Phys.* 100 (2006) 073706.
- [29] X. Liu, X. Xu and Y. Zhang, *Phys. Rev. B* 62 (2000) 15112.
- [30] L. S. Lakshmi, K. Dorr, K. Nenkov, V. Sridharan, V. S. Sastry, K. -H. Muller, *J. Magn. Mag. Mater.* 290-291(2005) 924; V. Sridharan, L. S. Lakshmi, R. Govindraj, R. Nithya, D. V. Natarajan and T. S. Radhakrishnan, *J. Alloys Comp.* 326 (2001) 65.
- [31] Y. H. Liu, B. -X. Huang, R. -Z. Zhang, X. -B. Yuan, C. -J. Wang and L. M. Mei, *J. Magn. Mag. Mater.* 293 (2005) 872.
- [32] J. S. Kim, D. C. Kim, G. C. McIntosh, S. W. Chu, Y. W. Park, B. J. Kim, Y. C. Kim, A. Maignan and B. Raveau, *Phys. Rev. B* 66 (2002) 224427.
- [33] I. O. Troyanchuk, M. V. Bushinsky, H. Szymazak, K. Barner, A. Maignan, *Eur. Phys. J. B*, 28 (2002) 75.
- [34] S. K. Agarwal, Neeraj Panwar, Vikram Sen and D. K. Pandya, *J. Phys. D: Appl. Phys.* 41 (2008) 105004.
- [35] V. Sen, Neeraj Panwar, G.L. Bhalla and S.K. Agarwal, *J. Alloys Compnd.* 439 (2007) 205.
- [36] V. Sen, Neeraj Panwar, G.L. Bhalla and S.K. Agarwal, *J. Phys. Chem. Solids* 68 (2007) 1685.
- [37] V. Sen, Neeraj Panwar, Ashok Rao, C.K. Hsu, Y.K. Kuo and S.K. Agarwal, *Solid State Communications* 145 (2008) 86.
- [38] V. Sen, G. L. Bhalla, Neeraj Panwar, W. K. Syu, N. Kaurav, Y. K. Kuo, Ashok Rao and S. K. Agarwal, *Physica B* 405 (2010) 1.
- [39] Y.-K. Kuo, C.S. Lue, F.H. Hsu, H.H. Li and H.D. Yang, *Phys. Rev. B* 64 (2001) 125124.
- [40] H. L. Ju, J. Gopalakrishnan, J. L. Peng, Q. Li, G. C. Xiong, T. Venkatesan, R. L. Greene, *Phys. Rev. B* 51 (1995) 6143.
- [41] Y. S. Nam, H. L. Ju and C.W. Park, *Solid State Commun.* 119 (2001) 613.
- [42] W. Zhong, W. Chen, C.T. Au, and Y.W. Du, *J. Magn. Magn. Mater.* 261. (2003) 238-243.
- [43] L. S. Lakshmi, K. Dorr, K. Nenkov, V. Sridharan, V.S. Sastry and K. H. Muller, *J. Mag. Magn. Mater.* 290-291 (2005) 924.

- [44] H. L. Ju, H. Sohn, *Solid State Commun.* 102 (1997) 463.
- [45] A. B. Beznosov, V. A. Desnenko, E. L. Fertman, C. Ritter and D. D. Khalyavin, *Phys. Rev. B* 68 (2003) 054109; N. Moutis, I. Panagiotopoulos, M. Pissas and D. Niarchos, *Phys. Rev. B* 59 (1999) 1129.
- [46] P. A. Lee and T. V. Ramakrishnan, *Rev. Mod. Phys.* 57 (1985) 287.
- [47] B. L. Altshuler and P. A. Lee, *Phys. Tod.* 41(1988) 36.
- [48] B. L. Altshuler and A. G. Aronov, in *electron-electron interactions in Disordered system*, (Eds.) A. L. Efros and M. Pollak (North-Holland, New York, 1985).
- [49] J. Kondo, *Prog. Theor. Phys.* 32 (1964) 37.
- [50] J. Kondo, *Solid State Physics*, 23 (1969) 183.
- [51] L. Kouwenhoven and L. Glazman, *Phys. World* 14 (2001) 33.
- [52] C. Kittel, *Introduction to Solid State Physics* (John Wiley & Sons, Singapore, 1995).
- [53] J. M. Ziman, *Electrons and Phonons* (Oxford University Press, London, 1967).
- [54] N. W. Ashcroft and N. D. Mermin, *Solid State Physics* (Saunders, Philadelphia, 1967).
- [55] I. Mannari, *Prog. Theo. Phys.* 22 (1959) 325.
- [56] T. Kasuya, *Prog. Theo. Phys.* 16 (1956) 58.
- [57] M. Viret, F. Ott, J. P. Renard, H. Glatli, L. P. -Gaudart and A. Revcolevschi, *Phys. Rev. Lett.* 93(2004) 27402.
- [58] M. G.-Hernandez, F. Guinea, A. de Andres, J. L. Martinez, C. Prieto and L. Vazquez, *Phys. Rev. B* 61 (2000) 9549; A. Maignan, C. Simon, V. Caignaert and B. Raveau, *J. Appl. Phys.* 79 (1996) 7891.
- [59] N. F. Mott, E. A. Davis, *Electronics Process in Noncrystalline Materials*, Clarendon, Oxford, 1971.
- [60] D. Emin, T. Holstein, *Studies of small-polaron motion IV. Adiabatic theory of Hall Effect*, *Ann. Phys.* 53 (1969) 439.
- [61] J. J. Hamilton, E. L. Keatley, H. L. Ju, A. K. Raychaudhuri, V. N. Smolyaninova, R. L. Greene, *Phys. Rev. B* 54 (1996) 14926.
- [62] H. Y. Hwang, S. -W. Cheong, N. P. Ong and B. Batlogg, *Phys. Rev. Lett.* 77 (1996) 2041.
- [63] F. J. Blatt, P. A. Schroeder, C. L. Foiles and D. Greig, in *Thermoelectric Power of Metals* (Plenum, New York), 1976.
- [64] A. Asamitsu, Y. Moritomo, and Y. Tokura, *Phys. Rev. B* 53 (1996) 2952.
- [65] A. J. Millis, P. B. Littlewood, B. I. Shraiman, *Phys. Rev. Lett.* 74 (1995) 5144.
- [66] N. F. Mott and E. A. Davis (Eds.), *Electronic Processes in Noncrystalline Materials*, Clarendon, Oxford, 1979.
- [67] K. Segal, Y. Kuroda and H. Sakata, *J. Mater. Sci.* 33 (1998) 1303.
- [68] A. Banerjee, S. Pal, S. Bhattacharya, B. K. Chaudhuri and H. D. Yang, *Phys. Rev. B* 64 (2001) 104428.
- [69] P. Mandal, *Phys. Rev. B* 61 (2000) 14675.
- [70] A. Urushibara, Y. Moritomo and Y. Tokura, *Phys. Rev. B* 51 (1995) 14103.
- [71] P. Dai, J. Zhang, H. A. Mook, S.-J. Lion, P. A. Dowben, and E. W. Plummer, *Phys. Rev. B* 54 (1996) 3694.
- [72] Y. Sun, X. Xu, and Y. Zhang, *Phys. Rev. B* 63 (2000) 054404.
- [73] D. W. Visser, A. P. Ramirez, M. A. Subramaniam, *Phys. Rev. Lett.* 78 (1997) 3947.

- [74] P. G. Klemens, in: F. Seitz, D. Turnbull (Eds.), *Solid State Physics*, Academic Press, New York, 1958, p 7.

IntechOpen

IntechOpen



**Advances in Ceramics - Electric and Magnetic Ceramics,
Bioceramics, Ceramics and Environment**

Edited by Prof. Costas Sikalidis

ISBN 978-953-307-350-7

Hard cover, 550 pages

Publisher InTech

Published online 06, September, 2011

Published in print edition September, 2011

The current book consists of twenty-four chapters divided into three sections. Section I includes fourteen chapters in electric and magnetic ceramics which deal with modern specific research on dielectrics and their applications, on nanodielectrics, on piezoceramics, on glass ceramics with para-, anti- or ferro-electric active phases, of varistors ceramics and magnetic ceramics. Section II includes seven chapters in bioceramics which include review information and research results/data on biocompatibility, on medical applications of alumina, zirconia, silicon nitride, ZrO₂, bioglass, apatite-wollastonite glass ceramic and b-tri-calcium phosphate. Section III includes three chapters in applications of ceramics in environmental improvement and protection, in water cleaning, in metal bearing wastes stabilization and in utilization of wastes from ceramic industry in concrete and concrete products.

How to reference

In order to correctly reference this scholarly work, feel free to copy and paste the following:

Neeraj Panwar, Indrani Coondoo, Vikram Sen and S. K. Agarwal (2011). Structural, Morphological, Magneto-Transport and Thermal Properties of Antimony Substituted (La,Pr)_{2/3}Ba_{1/3}Mn_{1-x}Sb_xO₃ Perovskite Manganites, *Advances in Ceramics - Electric and Magnetic Ceramics, Bioceramics, Ceramics and Environment*, Prof. Costas Sikalidis (Ed.), ISBN: 978-953-307-350-7, InTech, Available from: <http://www.intechopen.com/books/advances-in-ceramics-electric-and-magnetic-ceramics-bioceramics-ceramics-and-environment/structural-morphological-magneto-transport-and-thermal-properties-of-antimony-substituted-la-pr-2-3b>

INTECH
open science | open minds

InTech Europe

University Campus STeP Ri
Slavka Krautzeka 83/A
51000 Rijeka, Croatia
Phone: +385 (51) 770 447
Fax: +385 (51) 686 166
www.intechopen.com

InTech China

Unit 405, Office Block, Hotel Equatorial Shanghai
No.65, Yan An Road (West), Shanghai, 200040, China
中国上海市延安西路65号上海国际贵都大饭店办公楼405单元
Phone: +86-21-62489820
Fax: +86-21-62489821

© 2011 The Author(s). Licensee IntechOpen. This chapter is distributed under the terms of the [Creative Commons Attribution-NonCommercial-ShareAlike-3.0 License](#), which permits use, distribution and reproduction for non-commercial purposes, provided the original is properly cited and derivative works building on this content are distributed under the same license.

IntechOpen

IntechOpen